ARTICLE

A Si−O−C Composite Anode: High Capability and Proposed Mechanism of Lithium Storage Associated with Microstructural Characteristics

Hiroshi Fukui,[†] Hisashi Ohsuka,[†] Takakazu Hino,[†] and Kiyoshi Kanamura*[,‡]

Dow Corning Toray Company, Ltd., Chigusa-Kaigan, Ichihara 299-0108, Japan, and Department of Applied Chemistry, Graduate School of Urban Environmental Sciences, Tokyo Metropolitan University, Hachioji, Tokyo 192-0397, Japan

ABSTRACT A blend of phenyl-substituted, branched polysilane, $(Ph_2Si)_{0.85}(PhSi)_{0.15}$, and polystyrene (1:1 in weight) has been transformed into a composite material consisting of graphene layers, Si−O−C glasses, and micropores through a pyrolytic polymer-to-ceramic conversion. Several analytical techniques have been employed to characterize the Si−O−C composite material, demonstrating the presence of the three components in its host framework. The Si−O−C composite material performs well in electrochemical operations with a characteristic voltage plateau, offering a capacity of more than 600 mA h g^{-1}. When polystyrene is not blended, the resulting comparative material is even less porous and shows a shorter voltage plateau in electrochemical operations. A broad resonance in the ^{7}Li NMR spectrum recorded at low temperature can be deconvoluted into three components in the fully lithiated state of the Si−O−C composite material derived from the polymer blend. This result indicates that the Si−O−C composite material electrochemically stores lithium species in interstitial spaces or edges of the graphene layers, directly or indirectly the Si−O−C glass phase, and the micropores. However, both the Si−O−C glass phase and micropores are minor as electrochemically active sites for lithium storage, and interstitial spaces or edges of the graphene layers act as major electrochemically active sites in this composite material. Despite the excellent cyclability of the Si−O−C composite material, the voltage plateau disappeared over cycling. This phenomenon suggests that the microstructure is delicate for repetitive lithium insertion and extraction and that newly formed sites must generate the nearly equal capacity.

KEYWORDS: polysilane • pyrolysis • silicon oxycarbide • graphene layer • micropore • anode • lithium storage • rechargeable lithium battery

1. INTRODUCTION

Because of growing energy needs and environmental aspects, energy storage systems are in need of an advance in technology for popularization and spread in emerging fields such as automotive applications. Rechargeable lithium-ion batteries are the most promising candidates because of a high energy density but still have a challenge. Accordingly, extensive researches have been conducted on rechargeable lithium-ion batteries to further improve the performance such as energy density and cycling. Because a conventional anode material, graphite, almost attains its theoretical capacity (372 mA h g^{-1} in the form of LiC_6), much effort has been paid to yield new anode materials capable of offering a higher capacity (1). Among several alternatives, silicon oxycarbide (Si−O−C) glasses can be of much interest to us. In fact, many researchers have evaluated Si−O−C glasses as anode materials (2−12). According to these previous works, Si−O−C glasses have been shown to offer higher capacities (~920 mA h g^{-1}) than graphite. Unfortunately, however, Si−O−C glasses still need further improvement from an industrial point of view, suffering from a large irreversible capacity and poor cyclability. Carbon materials have been extensively studied as anode materials for rechargeable lithium-ion batteries (13), but there is no research to explain the origin of electrochemical lithium storage in Si−O−C glasses. It is believed that the reversible interplay between Si−O−C glasses and lithium ions occurs in electrochemical operations.

Other than the potential application as an anode material for rechargeable lithium-ion batteries, Si−O−C glasses have attracted much attention because of their fascinating physical and chemical properties (14−26). Replacing divalent oxygen atoms with tetravalent carbon atoms leads to more rigid and tough Si−O−C glasses. Because Si−O−C glasses usually contain free carbon as a second phase, along with a Si−O−C glass phase, another name they are known by is "black glasses". In general, Si−O−C glasses can be synthesized by pyrolysis of a wide variety of polymeric systems throughout polymer-to-ceramic conversion processes. Sol/gel precursors (14−22) and polysiloxane polymers (23−26) are particularly popular. Polysilane and polycarbosilane have also been known as important precursors to SiC (27−29).

* Corresponding author. E-mail: kanamura-kiyoshi@tmu.ac.jp.
Received for review October 7, 2009 and accepted February 24, 2010
[†] Dow Corning Toray Company, Ltd.
[‡] Tokyo Metropolitan University.
DOI: 10.1021/am100030f

Published on Web 03/10/2010

To tailor the chemical composition of Si−O−C glasses, several literature reports have described that the choice of prechar polymers is of importance. Organic substituents attached to polymer backbones have, in part, significance in tailoring the chemical composition (30, 31). Other than methyl groups, more carbon-rich substituents, ethyl, propyl, phenyl, and vinyl, have been introduced to polymer backbones (30, 31). If more free carbon-rich Si−O−C glasses are needed, phenyl and unsaturated groups, such as vinyl, are preferable. In contrast, because saturated alkyl chains are lost during pyrolysis, relatively low residual contents of free carbon can be realized in the final products. In some cases, free carbon may be undesired. The adjusted content of silicon, carbon, and oxygen in prechar polymers thus makes it possible to reduce the content of free carbon in Si−O−C glasses (32, 33). At higher temperatures (approximately >1300 °C), carbothermic reduction leads to the formation of SiC and turbostratic graphite from Si−O−C glasses through phase separation (14, 16, 18, 20, 31, 33). It is also known that the crystalline size of free carbon gradually becomes large in Si−O−C glasses with increasing heat treatment temperatures (HTTs) (20).

A Si−O−C composite material that we have found consists of (1) free carbon, (2) Si−O−C glasses, and (3) micropores (34). Both the free carbon and Si−O−C glasses are expected to electrochemically store lithium species. The expected role of the micropores is not only to increase the capacity as electrochemically active sites for lithium storage but also to maintain cyclability as alleviative sites for volume change. However, the micropores should not be major components from the standpoint of practical use. This is because high porosity fundamentally causes a low-density material, and it is eventually a disadvantage for preparing electrodes and batteries with a high energy density. To produce the Si−O−C composite material with the three components, phenyl-substituted, branched polysilane, $(Ph_2Si)_{0.85}(PhSi)_{0.15}$ (**1**), was employed as a prechar polymer. In addition, polystyrene was chosen as another prechar polymer. The two prechar polymers were blended with a weight ratio of 1:1 and then pyrolyzed at 1000 °C under an inert gas atmosphere. Polysilane **1** is expected to act not only as a silicon source but also as a free carbon one because it bears nothing but phenyl groups. Polystyrene is also a popular thermally degradable polymer expected to slightly yield the free carbon and form the micropores when it decomposes.

In this paper, structural analyses of the Si−O−C composite material with the three components are undertaken in depth using elemental analysis, powder X-ray diffraction (XRD), Raman spectroscopy, N_2 sorption isotherms, small-angle X-ray scattering (SAXS), ^{29}Si magic angle spinning nuclear magnetic resonance (MAS NMR) spectroscopy, scanning electron microscopy (SEM), energy-dispersive X-ray spectroscopy (EDS), transmission electron microscopy (TEM), electron energy loss spectroscopy (EELS), and high-angle annular dark-field scanning transmission electron microscopy (HAADF-STEM). A further effort is devoted to evaluation of the electrochemical lithium storage capability of this composite material to demonstrate the advantage of our material design. We also pay attention to ^{7}Li NMR analysis to gain beneficial information on its electrochemical lithium storage mechanism.

2. EXPERIMENTAL SECTION

2.1. Prechar Polymers. Polystyrene (average degree of polymerization = 2000) used in this study was purchased from Wako Pure Chemical Industries. Polysilane used in this study, $(Ph_2Si)_{0.85}(PhSi)_{0.15}$ (**1**), was kindly supplied by the Dow Corning Corp. This polysilane was used as received. Neither a product name nor a product number is given to **1** because it is a test sample. A typical polymer characteristic from gel permeation chromatography analysis (tetrahydrofuran, polystyrene standard) is $M_w = 1.03 \times 10^3$.

2.2. Preparation of the Polymer Blend. Polysilane **1** and polystyrene were dissolved with a weight ratio of 1:1 in toluene at 100 °C and then gently mixed with a rotary evaporator for 60 min. After evaporation of toluene, the polymer blend was further heated to remove residual toluene at 100 °C under vacuum. The resulting powdery sample was used for pyrolysis as a polymer blend.

2.3. Pyrolysis of the Prechar Polymer. The polymer blend (approximately 10 g) was placed in an alumina boat and then heat-treated to remove any possible decomposed byproduct, such as benzene and silane compounds, in a muffle furnace (NEMS, MT-400) at 600 °C (heating rate of 2 °C min^{-1}) under a nitrogen atmosphere (flow rate of 2000 mL min^{-1}) for 2 h. After heat treatment, the isolated char intermediate was milled (Itoh, VP-100) with a single zirconia ball (5-cm diameter) in air. The milled char intermediate was sieved with a 300 mesh. Eventually, the char intermediate (1 g) was placed in an alumina boat and then pyrolyzed in an alumina tube furnace at 1000 °C (heating rate of 5 °C min^{-1} from 100 °C, KRB-22HH, Isuzu Seisakusho) under an argon atmosphere (flow rate of 100 mL min^{-1}) for 1 h. Prior to pyrolysis, the tube furnace was always flushed with argon (purity of 99.999%) at a flow rate of 100 mL min^{-1} for 3 h. After the final temperature was kept for 1 h, the tube furnace was cooled down to <100 °C without control. The resulting Si−O−C composite material was named as PB. In this study, furthermore, polysilane **1** itself was also pyrolyzed in a similar way to yield a comparative material, PP. This allows us to obtain information about the effect of polystyrene on micropore formation.

2.4. Material Analysis. Elemental analysis (CHN, O, and Si) was performed at Sumika Chemical Analysis Service. The chemical composition of PB is $SiO_{0.51}C_{7.78}H_{0.49}$, and that of PP is $SiO_{0.61}C_{6.22}H_{0.78}$. There is no apparent reason to explain the incorporation of oxygen in both composite materials at present. Because the inert gases are not strictly pure, oxygen might leak in the furnaces during pyrolysis. The all-phenyl-substituted, branched backbone appears not to decompose exactly the same as dimethylpolysilane, which can be transformed into a Si−C−Si backbone through a methylene insertion at approximately 400 °C (27−29). The morphology of powdery samples was observed with a JEOL JSM-6490A (JEOL). Raman spectra were recorded on an NRS-1000 (Jasco) equipped with a microscope and a CCD detector. Excitation was by means of a green laser of 532 nm. Powder XRD patterns were measured on a RINT 2200 (Rigaku) equipped with an Ultima II+ high-resolution goniometer in the range of $2\theta = 10-90°$. Cu Kα radiation (1.5418 Å) was used as an X-ray source. A Belsorp mini II (BEL JAPAN) was employed to measure N_2 sorption isotherms at 77 K for open-pore characterization. The Brunauer−Emmett−Teller (BET) method was used to estimate the BET surface area (S_{BET}). The S_{BET} values of PB and PP are 14 and 4.2 m^2 g^{-1}, respectively. This difference would be caused by the decomposition of

polystyrene. A SAXS pattern of PB was obtained using a RINT Ultima III (Rigaku) equipped with transmission geometry in the range of $2\theta = 0.1-10°$. Cu Kα radiation (1.5418 Å) was used as an X-ray source. All paths in a receiving system to a detector were kept in vacuum so that X-rays are not scattered and adsorbed by air. ^{29}Si MAS NMR spectra were recorded on a Bruker AC300 spectrometer at 59.6 MHz. A pulse width of 3.40 μs ($\theta = 45°$) and a recycle delay of 30 s were used for single-pulse excitation without a cross-polarization technique. This will make it possible to gain at least general insight into the local environment of silicon in PB and PP. Powdery samples were placed in a 7-mm zirconia rotor and then spun with a seal at 4 kHz. All spectra were simulated with *WINFIT* software to quantitatively analyze the local environment of silicon. ^{29}Si NMR chemical shifts were referenced to external tetramethylsilane. TEM, EDS, EELS, and HAADF-STEM analyses were performed at Kobelco Research Institute.

2.5. Electrochemical Testing. The lithium storage capability of PB and PP was studied with 2016 coin-type cells. Prior to cell fabrication, a working electrode (14-mm diameter) was prepared in the following manner: (1) the active material, ketjen black (KB) as a conducting agent, and poly(vinylidene fluoride) (PVDF) as a binder were mixed with a weight ratio of 85:7.5:7.5; (2) the powdery mixture was appropriately dispersed in *N*-methyl-2-pyrrolidinone (NMP; Wako Pure Chemical); (3) the resulting slurry was applied on a copper foil; (4) the copper foil was placed in an oven at 85 °C under vacuum and then stored overnight to evaporate NMP; (5) the working electrode was cut away from the copper foil and then pressed at 20 MPa. The coin-type cells were fabricated with the working electrode, a lithium foil (15-mm diameter, Honjo Metal) as the counter electrode, and 1 mol dm^{-3} $LiPF_6$/ethylene carbonate and diethyl carbonate (1:1 in volume, Kishida Chemical) as the electrolyte in an argon-filled glovebox. A double-layered polypropylene sheet (Tonen Chemical) was sandwiched between the working and counter electrodes as a separator. In the range of 0−3 V, lithiation/delithiation testing was galvanostatically undertaken using an HJ1010mSM8A (Hokuto Denko) in a temperature-controlled bath (30 °C, FMO-133Z, Fukushima) at 37.2 mA g^{-1}. The average lithiation/delithiation capacities are shown with standard deviation. A rest period of 30 min was set at every lithiation/delithiation switch. Lithiation/delithiation cycle testing was performed in the same manner.

2.6. ^{7}Li NMR Analysis. A total of 2016 coin-type cells were fabricated in a way similar to that described above, with the exception that the active material, KB, and PVDF were mixed with a weight ratio of 85:5:10. The coin-type cells were short-circuited at least overnight to ensure the fully lithiated state of the active material and then dismantled in the glovebox. To draw the spectral change of PB at different states of lithiation and delithiation, several coin-type cells were carefully dismantled after reaching a given cell voltage at 18.6 mA g^{-1}. The working electrode was washed with dimethyl carbonate (DMC, Tomiyama Pure Chemical) and then transferred to a side chamber attached to the glovebox to evaporate DMC under vacuum. The resulting powdery sample was placed in a 7.5-mm Kel-F tube (JEOL), and then the sample tube was tightly sealed with a lid. ^{7}Li NMR spectra were acquired on a CMX-300 spectrometer (116.6 MHz, Chemagnetics) at room temperature. A 1 mol dm^{-3} aqueous LiCl solution was used as an external standard (0 ppm). A pulse width of 2.65 μs ($\theta = 90°$) and a recycle delay of 1 s were used for single-pulse excitation. To further analyze the fully lithiated PB, low-temperature measurements (−50, −90, and −120 °C) were conducted at Toray Research Center.

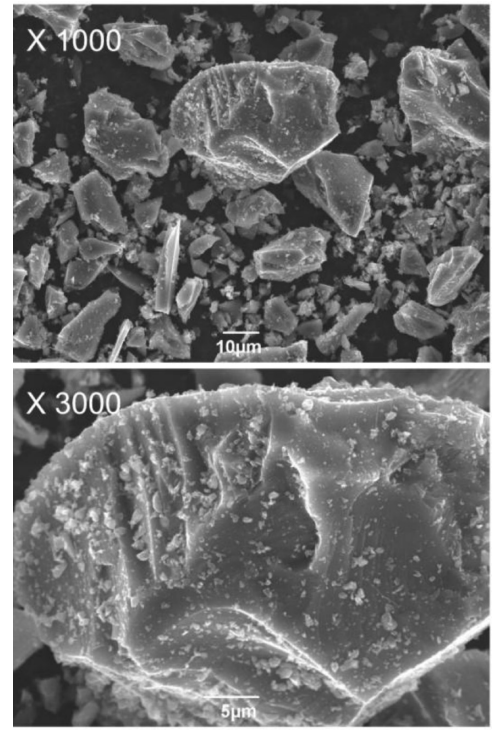

FIGURE 1. SEM images of PB.

3. RESULTS

3.1. Thermolysis. According to our thermal analysis (see Figure S1 in the Supporting Information), thermolysis of **1** and the polymer blend involves several stages in weight loss. A notable observation is that polysilane **1** and polystyrene have a major weight loss in almost the same temperature range. This thermolysis behavior is thought to be highly influential on micropore formation in the pyrolysis product. After heat treatment to 600 °C, polysilane **1** and the polymer blend both yielded an ocher monolith, and char yields became 47 and 26%, respectively. The difference in the char yield is reasonable because polystyrene contributes little to the char yield obtained from the polymer blend. Char yields after pyrolysis to 1000 °C became 96% in both prechar polymers. In the TGA curves (see Figure S1 in the Supporting Information), in fact, there exists little weight loss in a temperature range of 600−1000 °C.

3.2. SEM, Raman Spectroscopy, and XRD Measurements. Figure 1 presents the SEM images of PB. It can be seen that this composite material is made up of particles that are irregular in shape with partially rounded ones and large or submicrometer platelets. The surface of larger particles craters like "terraces", covered with tiny particles. Furthermore, cracks were also observed on the surface.

Raman spectroscopy is a powerful technique to evaluate graphitic structures in carbon materials. When HTT = 600 °C, the char intermediates for PB and PP showed no peaks in the range of 100−2100 cm^{-1}. This is probably due to the poor growth of the free carbon at this temperature. As shown in Figure 2a, two broad peaks can be seen in the Raman spectra of PB and PP. One is associated with the G band (E_{2g} mode), and the other is assigned to the D band (A_{1g} mode)

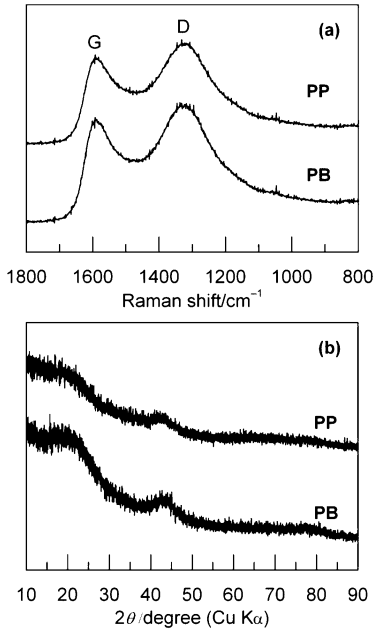

FIGURE 2. (a) Raman spectra and (b) XRD patterns of PB and PP.

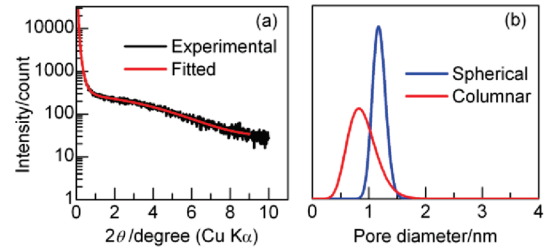

FIGURE 3. SAXS analysis results of PB: (a) SAXS pattern; (b) pore-size distribution calculated from part a.

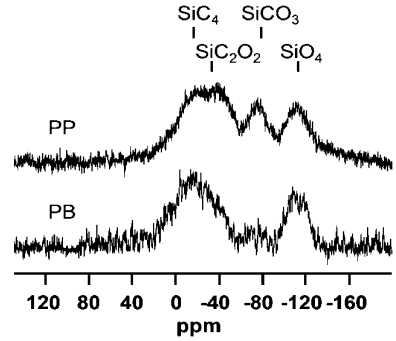

FIGURE 4. ^{29}Si MAS NMR spectra of PB and PP.

(35). The D band is known to appear in graphite with small particle sizes but not in large single crystals (35). According to the Raman spectra, PB and PP contain graphitic carbon. However, both composite materials show that the D band is more intense than the G band, thereby indicating that the edge density of graphitic carbon is high.

XRD analysis provides information on the crystalline structure of PB and PP. Figure 2b exhibits the XRD patterns of both composite materials. Because no sharp peaks can be seen, they have amorphous nature. A broad diffraction peak at $2\theta = 21-23°$ is associated with the Si−O−C glass (amorphous SiO_2) and graphitic carbon phases with high disorder in PB. Like hard carbon, graphitic carbon in PB likely forms graphene layers with stacking faults. PP shows a slightly different pattern, and this pattern difference signifies polystyrene-driven structural modification in the polymer blend.

3.3. SAXS Analysis. N_2 sorption isotherms provide information only on open pores accessible to N_2 molecules but not on closed pores (latent pores) (36, 37). Because closed pores are thought to be located next to the edges of neighboring graphene layers, other techniques are desired to analyze them. SAXS is known as a powerful tool to characterize closed-pore-size distributions, based on electron density contrast (38, 39). Figure 3a presents the SAXS pattern of PB. In the range of $2\theta = >1°$, the scattering pattern recorded was monotonic and showed no appreciable peaks. The pore-size distribution for PB was characterized by *NANO-Solver* software (40), where two types of scatterers, sphere and column, served as shape models. Figure 3b shows the pore-size distributions calculated for both spherical and columnar models. The spherical model offered a narrower pore-size distribution than the columnar one. In addition, the pore diameter was smaller in the columnar model than in the spherical one. However, both models indicate that the pore size in PB is in the range of <2-nm diameter in common. The pore diameters averaged 1.18 nm for the spherical model and 0.89 nm for the columnar one. The SAXS technique shows the presence of micropores in PB.

3.4. ^{29}Si MAS NMR Analysis. The local environment of silicon in Si−O−C glasses is also of great interest because it is believed that the Si−O−C glass phase acts as an electrochemically active site for lithium storage (2−12). ^{29}Si MAS NMR analysis was thus conducted for PB and PP (Figure 4). In general, all peaks broaden because of disordered structures having a large distribution of silicon units. A major ^{29}Si NMR resonance at −17 ppm in the spectrum of PB can be assigned to SiC_4 (66.3% in contribution). The presence of SiO_4 (26.4%) is seen at −110 ppm. In addition, a minor resonance corresponding to $SiCO_3$ (7.30%) can be visible at −69 ppm. In the spectrum of PP, a ^{29}Si NMR resonance ascribed to SiC_4 (38.0%) became less intense at −16 ppm. Instead, a new resonance appeared at −41 ppm, tentatively assigned to SiC_2O_2 (23.7%). Two more resonances can be seen at −75 ppm for $SiCO_3$ (12.0%) and −113 ppm for SiO_4 (26.3%). In both composite materials, no resonance associated with metallic silicon was observed (−80 ppm) (20).

3.5. EELS and HAADF Measurement. A focused ion beam (FIB) process was employed to prepare an approximately 100-nm-thick film of PB for EELS analysis. Over an area of 10 nm, as indicated in Figure 5a, EELS spectra, C K-edge, O K-edge, and Si L-edge, were measured (Figure 5b−d). In the C K-edge spectrum (Figure 5b), there exist two characteristic features at 285 and 291−310 eV. The former corresponds to a 1s−π^* loss peak as seen in graphite, and the latter corresponds to a 1s−σ^* loss peak as seen in diamondlike carbon (41). Any extra features are not displayed in the C K-edge spectrum. With reference to the spectrum of SiC, which is also displayed in Figure 5b for comparison, graphene layers are apparently one component

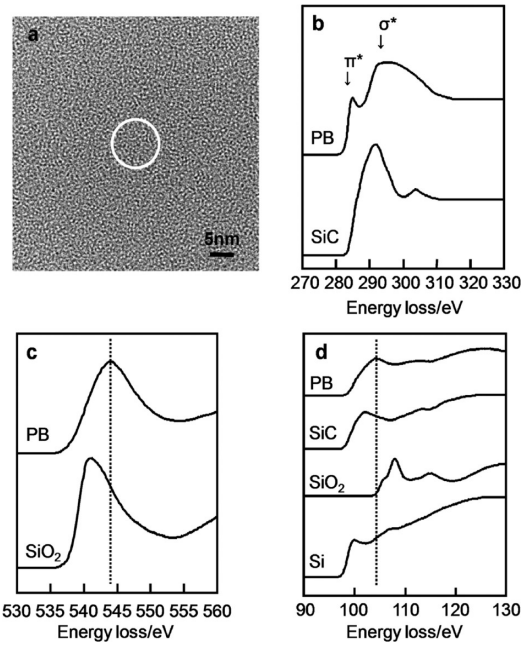

FIGURE 5. EELS analysis results of PB. (a) TEM image of a thin film of PB. The region indicated by a circle was analyzed with EELS. (b) C K-edge. (c) O K-edge. (d) Si L-edge. The spectra for SiC, SiO_2, and Si are also displayed for comparison.

in PB. The 1s−σ* loss peak broadens and thus indicates the existence of several types of tetrahedral carbon in PB. The O K-edge spectrum alone does not necessarily give much information, but PB has oxygen environments close to those of SiO_2 (Figure 5c). In the Si L-edge spectrum (Figure 5d), a broad feature was observed without clearly assignable peaks. According to the reference spectra displayed in Figure 5d, it can be seen that the silicon environments in PB encompass a variety of bonding types ranging from SiC to SiO_2. The environment of metallic silicon is, if any, very scarce, as identified in the ^{29}Si MAS NMR analysis.

HAADF imaging is capable of providing a *Z*-contrast image (*Z* is the atomic number) (42), allowing us to gain helpful information on chemical compositions. The FIB-processed thin film of PB was further analyzed with a HAADF-STEM technique. Figure 6a shows the HAADF-STEM image of PB. Brighter portions in the image can be considered as locations where heavier elements exist because the magnitude of brightness is approximately proportional to the square of *Z* (42). Because there is no large *Z* difference in PB (C, O, and Si), the image gave no strong contrasts in the thin film. To clarify the homogeneity of these three elements in PB, EDS analysis was conducted to capture elemental mappings for carbon, oxygen, and silicon in the thin film. It can be seen in Figure 6b−d that each element is homogeneously distributed without localization in the depth order of the thin film. This good homogeneity may deliver better electrochemical performance in rechargeable lithium-ion batteries.

3.6. Electrochemistry. The typical lithiation/delithiation profiles of PB are displayed in Figure 7. PB offers the first lithiation capacity of 867 ± 18 mA h g^{-1} and the first delithiation one of 608 ± 12 mA h g^{-1}. The first Coulombic efficiency of PB thus becomes approximately 70%. The SEI formation can be seen at around 0.9 V upon the first

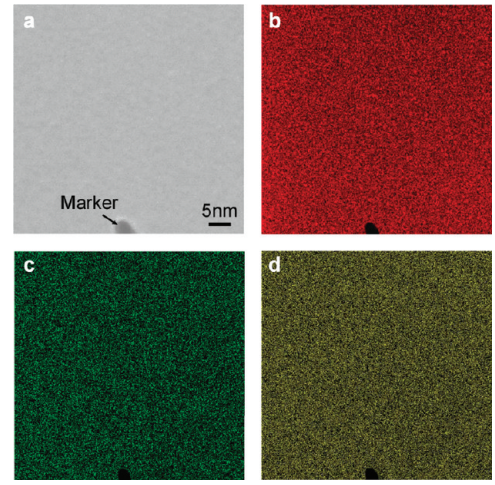

FIGURE 6. HAADF-STEM image and elemental mappings of a thin film of PB: (a) HAADF-STEM image; (b) carbon mapping; (c) oxygen mapping; (d) silicon mapping.

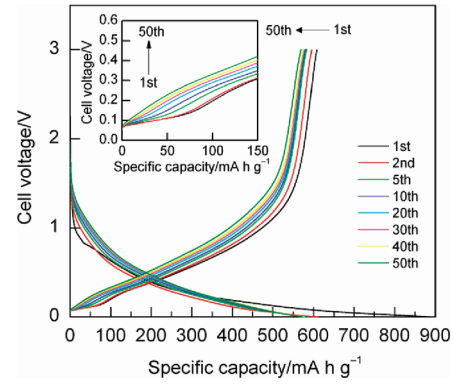

FIGURE 7. Selected lithiation/delithiation profiles of PB at the 1st, 2nd, 5th, and 10th−50th (every 10 cycles) cycles. The inset is the enlarged view of the delithiation profiles in the range of 0−150 mA h g^{-1}.

lithiation. A major irreversible reaction occurs over a wide range of voltages during the first lithiation. It is noteworthy that PB shows the most distinctive voltage plateau in the narrow range of approximately <0.1 V upon delithiation, thus indicating the presence of micropores where less ionic lithium species can be formed as seen in hard carbon (43−48). The voltage plateau corresponds to a delithiation capacity of approximately 80 mA h g^{-1}, not largely contributing to the total delithiation capacity. In the delithiation profile of PB, a slope other than the voltage plateau can be identified at approximately >0.1 V. Taking it into consideration, at least two electrochemically active sites are present in PB.

We believe that micropore incorporation contributes not only to increasing the capacity but also to prolonging the lithiation/delithiation cycle life by alleviating volume changes in repetitive lithium insertion and extraction. As shown in an inset of Figure 7, however, the voltage plateau tended to fade over cycling. Some structural changes are thus likely to occur by repetitive lithium insertion and extraction. It is worth noting that 95% of the first delithiation capacity (97% of the second delithiation capacity) was retained even after 40 cycles (Figure 8). This phenomenon is very interesting because some other forms of lithium species must offset the

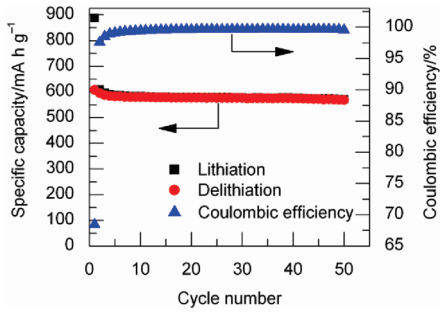

FIGURE 8. Lithiation/delithiation capacity and Coulombic efficiency vs cycle number.

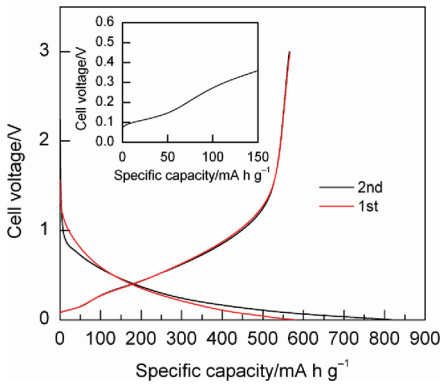

FIGURE 9. First and second lithiation/delithiation profiles of PP. The inset is the enlarged view of the first delithiation profile in the range of 0−150 mA h g^{-1}.

delithiation capacity originally delivered by less ionic lithium species in the micropores. Unfortunately, the fate of the micropores has remained uncertain.

Figure 9 exhibits the typical first and second lithiation/delithiation profiles of PP. The first lithiation and delithiation capacities of PP were 827 ± 9 and 573 ± 8 mA h g^{-1}, respectively, leading to the first Coulombic efficiency of approximately 70%. As a result, the first delithiation capacity of PP decreased by about 6%, compared to that of PB. The delithiation curves show that the voltage plateau unequivocally shortens, yielding a delithiation capacity of approximately 50 mA h g^{-1}. This capacity corresponds to approximately 60% of that observed in PB.

3.7. Room-Temperature ^{7}Li NMR Analysis. How PB and PP electrochemically store lithium remains an open question. The use of lithium nuclei as probes makes it possible to distinguish the local environment of lithium species in both composite materials. Figure 10a shows the ^{7}Li NMR spectrum of PB in a fully lithiated state at room temperature. The unsymmetrical shape of a broad peak suggests the presence of two or more electrochemically active sites for lithium storage in PB. The broad peak was thus deconvoluted into two Lorentzian components, one at a lower field (38 ppm, 79% in contribution) and the other at a higher field (14 ppm, 21%). For comparison, the ^{7}Li NMR spectrum of PP is displayed in Figure 10b. There was a clear difference between PB and PP in the ^{7}Li NMR spectra. In the ^{7}Li NMR spectrum of PP, the shape of a broad peak (approximately 20 ppm) was more symmetrical. The broad peak was deconvoluted into two Lorentzian components,

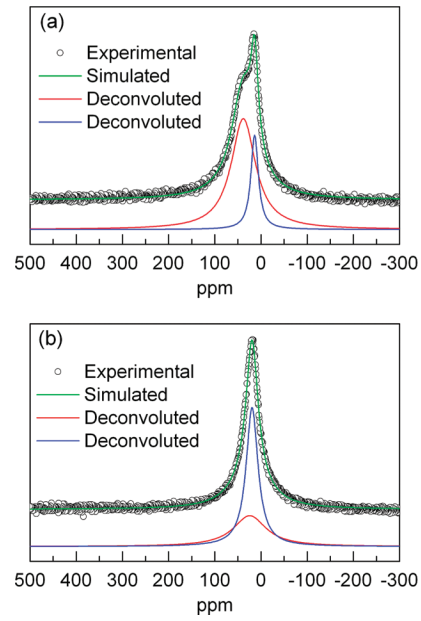

FIGURE 10. Room-temperature ^{7}Li NMR spectra of (a) PB and (b) PP in a fully lithiated state.

one at a lower field (24 ppm, 37%) and the other at a higher field (19 ppm, 63%). As for the lower and higher field peaks, there are large differences in resonance and contribution between the two composite materials.

3.8. Low-Temperature ^{7}Li NMR Analysis. ^{7}Li NMR resonances of lithiated hard carbon have been reported to be far more complicated at room temperature and highly dependent on the components of composite electrodes such as binders (49). It is thus difficult to interpret ^{7}Li NMR spectra obtained at room temperature in some cases. Meanwhile, it appears that ^{7}Li NMR spectra become much easier to interpret at low temperatures (49). Figure 11a presents the ^{7}Li NMR spectra of PB in a fully lithiated state at low temperatures. It is apparent that a shoulder peak shifted to lower fields with lowering temperatures. Unfortunately, using the ^{7}Li NMR spectra obtained at −90 and −120 °C, quantitative analysis may be uncertain at present. This is because the peak intensity of the lowest field peak (the shoulder peak) was so weak that difficulty was encountered in estimating the T_1 relaxation time and simulating by Lorentzian line shapes. Thus, the −50 °C spectrum was quantitatively analyzed, but the −90 and −120 °C spectra were qualitatively treated in this paper. In particular, the lowest field peak can be barely identified in the ^{7}Li NMR spectrum acquired at −120 °C.

Figure 11b exhibits a detailed view of the ^{7}Li NMR spectrum of PB obtained at −50 °C. As a result, the experimental peak was deconvoluted into three Lorentzian components (131, 18, and −21 ppm), indicating the presence of three electrochemically active sites for lithium storage in PB. The ^{7}Li NMR resonance at 131 ppm further shifted to a lower field, >200 ppm at −120 °C. The most intense ^{7}Li NMR resonance at 18 ppm hardly shifted even at −120 °C but just broadened. An additional resonance at −21 ppm led to a better simulation of the −50 °C spectrum (Figure 11b). As temperatures decreased to −90 and −120

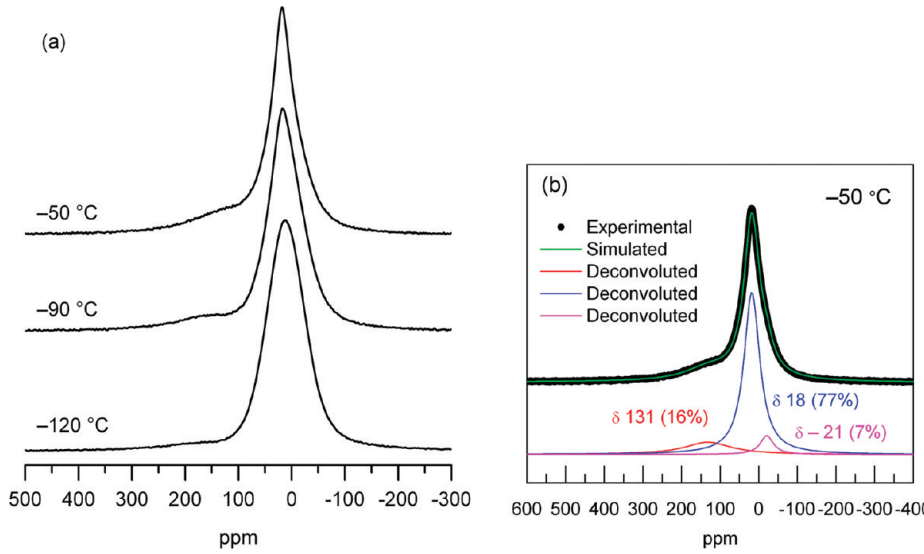

FIGURE 11. (a) Low-temperature ^{7}Li NMR spectra of PB in a fully lithiated state and (b) a detailed view of the spectrum measured at −50 °C. In the −50 °C spectrum (experimental), T_1 = 0.6 s (the major peak) and 0.8 s (the lowest field peak).

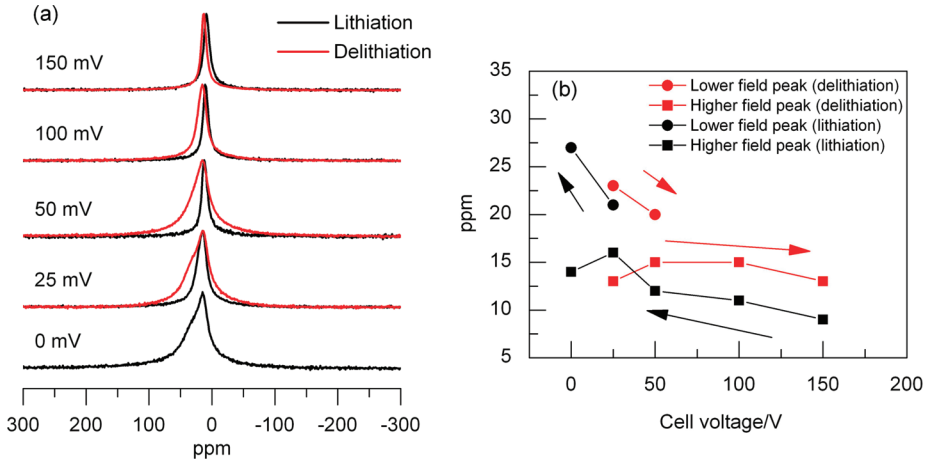

FIGURE 12. (a) Room-temperature ^{7}Li NMR spectra of PB at different cell voltages. For clarity, the spectra were normalized with the peak amplitude. (b) ^{7}Li NMR resonance changes vs cell voltages.

°C, the highest field peak became more intense, presumably owing to the short T_1 relaxation time.

3.9. ^{7}Li NMR Resonance vs Cell Voltage. Further ^{7}Li NMR analysis was undertaken to understand how lithium species are inserted into and extracted from PB at room temperature. At lower cell voltages, the local environment of lithium species should be liable to variation. Thus, ^{7}Li NMR spectra were acquired in the most informative range of 0−150 mV. Figure 12 displays the ^{7}Li NMR spectra and resonance changes of PB at different cell voltages. The symmetrical shape of a peak centered at 9−12 ppm can be seen at 50−150 mV upon lithiation. It is also evident from Figure 12a that a shoulder peak becomes more discernible with lowering cell voltages (lithiation). A further cathodic reduction to 0 mV led to another peak at 27 ppm.

Compared with the ^{7}Li NMR spectrum shown in Figure 10a, the newly emerged resonance (the shoulder peak) shifted to a higher field at 0 mV (38−27 ppm). This is because the ^{7}Li NMR spectrum at 0 mV was not necessarily obtained in a fully lithiated state. In other words, each cell voltage is far from equilibrium. Upon delithiation, in fact, a hysteresis was observed in the ^{7}Li NMR spectra. At 50 mV, the shoulder peak can be unambiguously seen in the direction of delithiation. This is also explained by polarization behaviors as mentioned above. As shown in Figure 7, once the cell voltage reaches 0 V, it tends to quickly elevate during rest periods taken in each lithiation/delithiation switch. The shoulder peak almost disappeared at 100 mV upon delithiation.

4. DISCUSSION

4.1. Composition and Microstructure. Si−O−C glasses have higher capacities than graphite, but their poor cyclability and large irreversible capacity are disadvantages in practical use. In this study, the formation of micropores is thought to deliver advantages, such as increasing the capacity and prolonging the cycle life, in Si−O−C glasses. First, efforts were thus made to understand the composition and microstructure of our Si−O−C composite materials.

Assuming that the general formula $SiC_xO_{2(1-x)} + yC$ (free carbon) (20) is applicable to PB and PP, the chemical compositions indicate that both composite materials have

$SiC_{0.75}O_{0.51}$ + 7.03C and $SiC_{0.70}O_{0.61}$ + 5.52C, respectively. The free carbon is present in PB and PP, but the difference in y is not small. This result suggests that polystyrene provides part of the free carbon through its thermal decomposition. The Raman spectra of PB and PP exhibiting two broad bands (G and D) evidence that the free carbon is composed of graphene layers with a high edge density. This result is in good agreement with the presence of the 1s−π^* loss peak in the EELS spectrum of C K-edge for PB. The XRD patterns of PB and PP show that both composite materials are featureless in a long-range order and that the stacking of the graphene layers is quite small in extent. The disordered structures of PB and PP are reasonable because of the low-temperature treatment of the prechar polymers and are similar to the characteristics of hard carbon. The SiC crystallization through carbothermic reduction does not occur at 1000 °C (14, 16, 18, 20, 31, 33).

Open and closed porosities should be handled separately here. Considering decomposition of the electrolyte, leading to irreversible capacities upon the initial lithiation, the surface area should be small. According to the N_2 sorption isotherm, the S_{BET} values of PB and PP are relatively small. Because of the sensitivity of open porosity, unfortunately, it is difficult to compare the surface areas of PB and PP with those of the previously reported carbon materials (46) and Si−O−C glasses (12). If PB and PP have closed pores located next to the edges of neighboring graphene layers, SAXS analysis should give helpful information on the pore-size distribution. Closed pores with appropriate sizes are expected to act as electrochemically active ones that reversibly store lithium species. As shown in Figure 3b, our simulated SAXS pattern confirms that there are micropores (<2-nm diameter) in PB with two shape models.

The ^{29}Si MAS NMR and EELS analyses demonstrate that most, if not all, of the Si−Si bonds are cleaved in **1** during pyrolysis to 1000 °C. On the surface of PB and PP, our XPS analysis confirms that silicon is bound to three or four oxygen atoms (see Figure S2 in the Supporting Information). It is reasonable to assume an oxidized surface state because the char intermediates were mechanically pulverized in air. In a short-range order in the inside of PB and PP, on the other hand, several SiC_xO_{4-x} (x = 0, 1, and 4 in PB and x = 0, 1, 2, and 4 in PP) environments can be seen, as shown in the ^{29}Si MAS NMR spectra (Figure 4). The broad environment of silicon in PB is also evidenced by the Si L-edge spectrum (Figure 5d). In the ^{29}Si MAS NMR spectrum of PP, the assignment of the broad resonance at approximately 40 ppm is uncertain and some overlapped peaks may thus be included. Although the Si−O−C glass phases are not exactly the same, however, PB and PP have a random distribution of Si−O and Si−C bonds in the glass phases. This agrees with the mapping result of carbon, oxygen, and silicon in the thin film of PB (Figure 6b−d).

4.2. Lithium Storage and Mechanism. Compared to hard carbon, in the delithiation profile of PB (Figure 7), the contribution (80 mA h g^{-1}) of the characteristic voltage plateau at approximately <0.1 V appears to be small (43−48). It is thus deduced that PB is less porous than hard carbon from an electrochemical point of view. In this regard, however, PP is even less likely to be porous with a contribution of 50 mA h g^{-1}. This raises a question on what contributes most to the rest of the delithiation capacity (>500 mA h g^{-1}). In general, micropores are known to be located next to the edges of neighboring graphene layers in hard carbon (43−48, 50). In addition, it is reasonable that graphite-like ordering cannot be realized in hard carbon even at high HTTs because of its intrinsic nature. Nevertheless, it is not necessarily correct that graphene layers have no stacking order. It has been reported that hard carbon is capable of storing lithium species not only in micropores but also in interstitial spaces of graphene layers (43−48, 50). Accordingly, lithium species could be intercalated into graphene layers of PB and PP in a similar manner.

According to the ^{7}Li NMR spectra of PB and PP in a fully lithiated state (Figure 10), it is obvious that there are at least two different environments of lithium species in both composite materials. Considering that lithiated hard carbon presents a similar ^{7}Li NMR resonance at a relatively low field as well as a voltage plateau (43), less ionic lithium species could be stored in micropores of PB and PP. The differences in resonance (38 ppm for PB and 24 ppm for PP) and contribution (79% for PB and 37% for PP) of the lower field peaks are significant. The electrochemically active pores are thus more likely minor components in PP than in PB. This idea agrees with the difference in contribution of the voltage plateau. The following can be understood from these results: (1) polystyrene plays a key role in incorporating micropores into a Si−O−C host framework as expected; (2) phenyl groups of **1** also contribute to the formation of micropores to a certain extent.

It is also known that the ^{7}Li NMR resonance ascribed to less ionic lithium species in lithiated hard carbon shifts to considerably lower fields at low temperatures because of the slow exchange of lithium nuclei (49, 51, 52). Therefore, the lower field peak shown in Figure 10 could represent an exchange of lithium nuclei in two or more different electrochemically active sites for lithium storage. If an exchange of lithium nuclei occurs in both composite materials, a similar phenomenon should be observed in our ^{7}Li NMR analysis at low temperatures. To clarify a possible exchange of lithium nuclei in PB, ^{7}Li NMR analysis was conducted at low temperatures (−50, −90, and −120 °C).

As the temperatures are decreased, the shape of a broad peak changes in the ^{7}Li NMR spectra of PB (Figure 11a). Of course, diamagnetic lithium species, such as LiOH and Li_2O, could contribute to the broad peak. In fact, only one ^{7}Li NMR resonance was observed at approximately 0 ppm after delithiation to 3 V (see Figure S3 in the Supporting Information), usually assigned to these types of lithium species. However, it has been reported that the diamagnetic lithium species have much longer T_1 relaxation times than paramagnetic ones (45). We thus assume that our measurement condition suppresses the contribution of the diamagnetic lithium species particularly at lower temperatures and that

they, if any, will have a minimum impact on the ^{7}Li NMR spectra discussed in this paper.

The ^{7}Li NMR resonance at 131 ppm (Figure 11b) is similar to that reported in lithiated hard carbon, generally assigned to less ionic lithium species (45, 49, 51, 52). The most distinguishing behavior of less ionic lithium species is evidenced by the Knight shift. In fact, this prominent ^{7}Li NMR resonance further shifted to a lower field, >200 ppm at −120 °C. Therefore, the lowest field peak could be ascribed to less ionic lithium species in micropores of PB.

The ^{7}Li NMR resonance at 18 ppm just broadened as the temperatures were decreased. A similar resonance is known to be associated with lithium species intercalated into graphene layers of hard carbon (51, 52) and soft carbon (53), or stored in the edges (49, 54). In PB, thus, interstitial spaces of graphene layers or the edges could be major lithium storage sites. Our result also suggests that the motion of such lithium species freezes with lowering temperatures. Little shift of the 18 ppm resonance is likely unusual because lithiated hard carbon shows exchange of lithium nuclei between micropores and interstitial spaces of graphene layers (51, 52) or the edges (49). This may mean that lithium species in interstitial spaces of graphene layers or the edges scarcely participate in an exchange of lithium nuclei in PB.

If the lowest field peak at ≥131 ppm is a component of the mean peak at 38 ppm observed at room temperature (Figure 10a), a counterpeak must concomitantly appear in the ^{7}Li NMR spectra at low temperatures. The additional resonance at −21 ppm, which is assigned to lithium species in a highly shielded environment, was fitted well as a component in Figure 11b. Because the fully lithiated PB was washed with DMC, the highest field peak is not assigned to lithium species of the electrolyte. In addition, lithium species of the SEI usually do not cause it. If the lithium species assignable to the −21 ppm resonance take part in an exchange of lithium nuclei, they would be located close to less ionic lithium species in the micropores. On the basis of our structural analysis results, PB consists of three components, of which interstitial spaces of graphene layers or the edges and micropores, as discussed, could act as electrochemically active sites for lithium storage. The third component turns out to be Si−O−C glasses. Because these three components are homogeneously dispersed in PB, the highest field peak may be related to the interplay between the Si−O−C glass phase and lithium ions. Recently, Key et al. have reported that lithiated silicon with the metastable phase of $Li_{15}Si_4$ shows the ^{7}Li NMR resonance at −10 ppm (55). Interestingly, while the XPS Si 2p spectra of a PB electrode exhibit a broad peak centered at approximately 100 eV in a fully lithiated state (see Figure S4 in the Supporting Information), the Si 2p binding energy of the PB electrode is 102−103 eV before lithiation (see Figure S4 in the Supporting Information). The lower binding energy after lithiation suggests the formation of different silicon components containing Si−C and Si−Si bonds in PB. Concomitantly with the binding energy change in silicon, the XPS O 1s spectra of the PB electrode indicate the formation of Li_2O after lithiation (see Figure S5 in the Supporting Information). At present, the −21 ppm resonance could arise from highly diamagnetic lithium species in a similar lithiated silicon phase newly emerged in PB after reductive cleavage of the Si−O bonds in the Si−O−C glass phase upon lithiation. Considering the contribution of the −21 ppm resonance, the Si−O−C glass phase is thought to be minor as an electrochemically active site for lithium storage in PB.

The spectral and resonance changes in Figure 12 indicate that lithium species are first intercalated into graphene layers of PB or stored in the edges, and then less ionic lithium species are inserted into micropores of PB at quite low cell voltages, as previously suggested in hard carbon (43, 56). Given that an exchange of lithium nuclei was observed, it is probable that the lithium species associated with the −21 ppm resonance (Figure 11b) are present in PB at 25 mV upon lithiation. In the direction of delithiation, the disappearance of the shoulder peak at 100 mV is of note. This result confirms that the voltage plateau terminates at approximately 100 mV during delithiation in Figure 7 and corresponds to the extraction of less ionic lithium species in micropores of PB. A further delithiation to 150 mV gives nearly the same spectrum as that obtained upon lithiation. Our ^{7}Li NMR analysis reveals that lithium species are reversibly inserted into and extracted from respective sites in PB, consequently resulting in a delithiation capacity of approximately 600 mA h g^{-1}.

It should be noted that the voltage plateau is no longer visible in the delithiation profiles of PB after several tens of cycles (Figure 7). As mentioned above, the voltage plateau is apparently associated with the extraction of less ionic lithium species in micropores of PB. The disappearance of the voltage plateau suggests that PB has a delicate microstructure affected by repetitive lithium insertion and extraction. At the moment, of course, we cannot exclude that the micropores merely lost electrochemical activities for lithium storage and are still present in PB. Further studies are needed to clarify the fate of the micropores over cycling.

According to the previous study (12), the Si−O−C glass phase is of major significance in both reversible and irreversible capacities. In light of the electrochemical performance, thus, the fraction of the three components (free carbon, Si−O−C glasses, and micropores) needs to be studied in more detail for optimization. Although the initial irreversible capacity must still be decreased as much as possible for practical use, the excellent cycle life demonstrates that PB is a promising candidate as an anode material for advanced batteries (57), ensuring well-balanced capability (high capacity and excellent cyclability) in electrochemical lithium storage.

5. CONCLUSION

A blend of phenyl-substituted, branched polysilane, $(Ph_2Si)_{0.85}(PhSi)_{0.15}$, and polystyrene (1:1 in weight) has been used to prepare a Si−O−C composite as an anode material for rechargeable lithium-ion batteries. Structural analyses, using ^{29}Si MAS NMR, XRD, Raman spectroscopy, SAXS, TEM, and EELS, confirm that the Si−O−C composite ma-

terial has an amorphous nature with the following components: graphene layers (free carbon), Si−O−C glasses, and micropores (closed pores). Elemental analysis indicates that the Si−O−C composite material is considerably free carbon-rich. In the delithiation profiles of the Si−O−C composite material, a voltage plateau can be seen at approximately <0.1 V, indicating that the micropores act as electrochemically active sites where less ionic lithium species can be formed. Low-temperature ^{7}Li NMR analysis suggests the presence of three electrochemically active sites for lithium storage in the Si−O−C composite material. A major lithium storage site could be interstitial spaces or edges of the graphene layers. A characteristic ^{7}Li NMR resonance assignable to less ionic lithium species in the electrochemically active pores considerably shifts to lower fields (131 to >200 ppm) at low temperatures. Nevertheless, the intensity of the ^{7}Li NMR resonance is weak in the Si−O−C composite material, indicating that less ionic lithium species play a minor role in generating reversible capacities. A notable but less intense ^{7}Li NMR resonance associated with highly diamagnetic lithium species suggests the direct or indirect lithium storage in the Si−O−C glass phase as a minor electrochemically active site.

The voltage plateau tended to vanish away through lithiation/delithiation cycling. However, interestingly, the initial capacity almost remained in the Si−O−C composite material even after 40 cycles. Thus, some structural changes are likely to occur by repetitive lithium insertion and extraction. This result suggests the emergence of some other forms of lithium species substituted for less ionic lithium ones in the electrochemically active pores.

Acknowledgment. The authors acknowledge Dr. Kuniaki Tatsumi, Miyuki Nakajima, and Dr. Hikari Sakaebe of the National Institute of Advanced Industrial Science and Technology for beneficial discussion and technical assistance on ^{7}Li NMR measurement. We also thank Katsuya Eguchi of Dow Corning Toray Co., Ltd., for ^{29}Si MAS NMR measurement and Rigaku Corp. for SAXS analysis.

Supporting Information Available: Additional experimental information, TGA/DTA curves of **1** and the polymer blend to 900 °C, XPS spectra (C 1s, O 1s, and Si 2p) of PB and PP, ^{7}Li NMR spectrum of PB after delithiation to 3 V, XPS spectra (Si 2p and O 1s) of a PB electrode before lithium insertion, and XPS spectra (Si 2p and O 1s) of a PB electrode after lithium insertion. This material is available free of charge via the Internet at http://pubs.acs.org.

REFERENCES AND NOTES

(1) Tarascon, J.-M.; Armand, M. *Nature* **2001**, *414*, 359–367.
(2) Xing, W.; Wilson, A. M.; Zank, G.; Dahn, J. R. *Solid State Ionics* **1997**, *93*, 239–244.
(3) Xing, W.; Wilson, A. M.; Eguchi, K.; Zank, G.; Dahn, J. R. *J. Electrochem. Soc.* **1997**, *144*, 2410–2416.
(4) Wilson, A. M.; Zank, G.; Eguchi, K.; Xing, W.; Yates, B.; Dahn, J. R. *Chem. Mater.* **1997**, *9*, 1601–1606.
(5) Tamai, H.; Sugahara, H.; Yasuda, H. *J. Mater. Sci. Lett.* **2000**, *19*, 53–56.
(6) Mukai, S. R.; Yamamoto, Y.; Masuda, T.; Tamon, H. *Kagaku Kogaku Ronbunshu* **2003**, *29*, 221–225.
(7) Ning, L. J.; Wu, Y. P.; Wang, L. Z.; Fang, S. B.; Holze, R. *J. Solid State Electrochem.* **2005**, *9*, 520–523.
(8) Konno, H.; Morishita, T.; Sato, S.; Habazaki, H.; Inagaki, M. *Carbon* **2005**, *43*, 1111–1114.
(9) Wilson, A. M.; Xing, W.; Zank, G.; Yates, B.; Dahn, J. R. *Solid State Ionics* **1997**, *100*, 259–266.
(10) Wilson, A. M.; Zank, G.; Eguchi, K.; Xing, W.; Dahn, J. R. *J. Power Sources* **1997**, *68*, 195–200.
(11) Wilson, A. M.; Zank, G.; Eguchi, K.; Xing, W.; Yates, B.; Dahn, J. R. *Chem. Mater.* **1997**, *9*, 2139–2144.
(12) Larcher, D.; Mudalige, C.; George, A. E.; Porter, V.; Gharghouri, M.; Dahn, J. R. *Solid State Ionics* **1999**, *122*, 71–83.
(13) Dahn, J. R.; Zheng, T.; Liu, Y.; Xue, J. S. *Science* **1995**, *270*, 590–593.
(14) Babonneau, F.; Thorne, K.; Mackenzie, J. D. *Chem. Mater.* **1989**, *1*, 554–558.
(15) Zhang, H.; Pantano, C. G. *J. Am. Ceram. Soc.* **1990**, *73*, 958–963.
(16) Belot, V.; Corriu, R. J. P.; Leclercq, D.; Mutin, P. H.; Vioux, A. *J. Non-Cryst. Solids* **1992**, *144*, 287–297.
(17) Babonneau, F.; Bois, L.; Livage, J. *J. Non-Cryst. Solids* **1992**, *147−148*, 280–284.
(18) Babonneau, F.; Bois, L.; Yang, C.-Y.; Interrante, L. V. *Chem. Mater.* **1994**, *6*, 51–57.
(19) Bois, L.; Maquet, J.; Babonneau, F.; Mutin, H.; Bahloul, D. *Chem. Mater.* **1994**, *6*, 796–802.
(20) Sorarù, G. D.; D'Andrea, G.; Campostrini, R.; Babonneau, F.; Mariotto, G. *J. Am. Ceram. Soc.* **1995**, *78*, 379–387.
(21) Campostrini, R.; D'Andrea, G.; Carturan, G.; Ceccato, R.; Sorarù, G. D. *J. Mater. Chem.* **1996**, *6*, 585–594.
(22) Liu, Q.; Shi, W.; Babonneau, F.; Interrante, L. V. *Chem. Mater.* **1997**, *9*, 2434–2441.
(23) Corriu, R. J. P.; Leclercq, D.; Mutin, P. H.; Vioux, A. *J. Mater. Sci.* **1995**, *30*, 2313–2318.
(24) Wild, M. J.; Buhler, P. *J. Mater. Sci.* **1998**, *33*, 5441–5444.
(25) Schiavon, M. A.; Redondo, S. U. A.; Pina, S. R. O.; Yoshida, I. V. P. *J. Non-Cryst. Solids* **2002**, *304*, 92–100.
(26) Kolář, F.; Machovič, V.; Svítilová, J.; Borecká, L. *Mater. Chem. Phys.* **2004**, *86*, 88–98.
(27) Yajima, S.; Hayashi, J.; Omori, M.; Okamura, K. *Nature* **1976**, *261*, 683–685.
(28) Carlsson, D. J.; Cooney, J. D.; Gauthier, S.; Worsfold, D. J. *J. Am. Ceram. Soc.* **1990**, *73*, 237–241.
(29) Schmidt, W. R.; Interrante, L. V.; Doremus, R. H.; Trout, T. K.; Marchetti, P. S.; Maciel, G. E. *Chem. Mater.* **1991**, *3*, 257−267.
(30) White, D. A.; Oleff, S. M.; Fox, J. R. *Adv. Ceram. Mater.* **1987**, *2*, 53–59.
(31) Burns, G. T.; Taylor, R. B.; Xu, Y.; Zangvil, A.; Zank, G. A. *Chem. Mater.* **1992**, *4*, 1313–1323.
(32) Babonneau, F.; Sorarù, G. D.; D'Andrea, G.; Diré, S.; Bois, L. *Mater. Res. Soc. Symp. Proc.* **1992**, *271*, 789–794.
(33) Singh, A. K.; Pantano, C. G. *Mater. Res. Soc. Symp. Proc.* **1992**, *271*, 795–800.
(34) Fukui, H.; Ohsuka, H.; Hino, T.; Kanamura, K. *Chem. Lett.* **2009**, 86–87.
(35) Matthews, M. J.; Pimenta, M. A.; Dresselhaus, G.; Dresselhaus, M. S.; Endo, M. *Phys. Rev. B* **1999**, *59*, 6585–6588.
(36) From an electrochemical aspect (potential SEI formation accompanied by irreversible lithium consumption), less open pores would be favored.
(37) Rouquerol, F.; Rouquerol, J.; Sing, K. *Adsorption by Powders and Porous Solids*; Academic Press: London, 1999.
(38) Fukuyama, K.; Kasahara, Y.; Kasahara, N.; Oya, A.; Nishikawa, K. *Carbon* **2001**, *39*, 287–290.
(39) Omote, K.; Ito, Y.; Kawamura, S. *Appl. Phys. Lett.* **2003**, *82*, 544–546.
(40) *NANO-Solver* on the website http://www.rigaku.com/software/nanosolver.html.
(41) Amaratunga, G. A. J.; Chhowalla, M.; Kiely, C. J.; Alexandrou, I.; Aharonov, R.; Devenish, R. M. *Nature* **1996**, *383*, 321–323.
(42) Carlino, E.; Grillo, V. *Phys. Rev. B* **2005**, *71*, 235303.
(43) Alcántara, R.; Ortiz, G. F.; Lavela, P.; Tirado, J. L.; Stoyanova, R.; Zhecheva, E. *Chem. Mater.* **2006**, *18*, 2293–2301.
(44) Nagao, M.; Pitteloud, C.; Kamiyama, T.; Otomo, T.; Itoh, K.; Fukunaga, T.; Tatsumi, K.; Kanno, R. *J. Electrochem. Soc.* **2006**, *153*, A914–A919.
(45) Letellier, M.; Chevallier, F.; Béguin, F.; Frackowiak, E.; Rouzaud, J.-N. *J. Phys. Chem. Solids* **2004**, *65*, 245–251.

(46) Xing, W.; Xue, J. S.; Zheng, T.; Gibaud, A.; Dahn, J. R. *J. Electrochem. Soc.* **1996**, *143*, 3482–3491.
(47) Peled, E.; Eshkenazi, V.; Rosenberg, Y. *J. Power Sources* **1998**, *76*, 153–158.
(48) Buiel, E.; George, A. E.; Dahn, J. R. *J. Electrochem. Soc.* **1998**, *145*, 2252–2257.
(49) Guérin, K.; Ménétrier, M.; Février-Bouvier, A.; Flandrois, S.; Simon, B.; Biensan, P. *Solid State Ionics* **2000**, *127*, 187–198.
(50) Azuma, H.; Imoto, H.; Yamada, S.; Sekai, K. *J. Power Sources* **1999**, *81*−*82*, 1–7.
(51) Tatsumi, K.; Conard, J.; Nakahara, M.; Menu, S.; Lauginie, P.; Sawada, Y.; Ogumi, Z. *Chem. Commun.* **1997**, 687–688.
(52) Tatsumi, K.; Conard, J.; Nakahara, M.; Menu, S.; Lauginie, P.; Sawada, Y.; Ogumi, Z. *J. Power Sources* **1999**, *81*−*82*, 397–400.
(53) Tatsumi, K.; Akai, T.; Imamura, T.; Zaghib, K.; Iwashita, N.; Higuchi, S.; Sawada, Y. *J. Electrochem. Soc.* **1996**, *143*, 1923–1930 .
(54) Dai, Y.; Wang, Y.; Eshkenazi, V.; Peled, E.; Greenbaum, S. G. *J. Electrochem. Soc.* **1998**, *145*, 1179–1183.
(55) Key, B.; Bhattacharyya, R.; Morcrette, M.; Seznéc, V.; Tarascon, J.-M.; Grey, C. P. *J. Am. Chem. Soc.* **2009**, *131*, 9239–9249.
(56) Tatsumi, K.; Kawamura, T.; Higuchi, S.; Hosotubo, T.; Nakajima, H.; Sawada, Y. *J. Power Sources* **1997**, *68*, 263–266.
(57) We need to see which application is best suited to PB. Considering the energy density of rechargeable lithium-ion batteries, this composite material may be awkward to use in consumer applications such as portable devices. Because the rate capability of PB is likely to be high, it may meet the needs of specific applications such as hybrid electric vehicles.

AM100030F